CrossMark

Microstructural Characterization of Yttria-Stabilized Zirconia Sintered at Different Temperatures Using 3D EBSD, 2D EBSD and Stereological Calculations

Piotr Bobrowski, Marek Faryna, and Zbigniew Pędzich

A set of yttria-stabilized zirconia samples sintered at increasing temperatures was investigated using two-dimensional (2D) and three-dimensional (3D) electron backscatter diffraction (EBSD) techniques to calculate grain size distributions and grain boundary densities. The obtained results were compared to the results of stereological calculations and revealed that mean intercept length, a commonly used stereological parameter, is ca. 20% lower than an average grain diameter derived from 2D and 3D EBSD data. Moreover, the results based on 2D and 3D EBSD analyses were similar to each other in grain boundary density, while the values obtained from the stereological approach were noticeably lower.

1. Introduction

Several properties of polycrystalline materials such as strength, toughness, electrical conductivity and diffusivity are influenced by properties of grain boundaries (Ref 1). Their structure also influences grain growth and corrosion processes (Ref 2). In case of zirconia ceramics, the investigation of grain boundary structure and understanding the grain boundaries will allow for better controlling of sintering process and optimizing sintered material properties (Ref 3, 4). Many important applications of zirconia, e.g., as cutting tool material, exploit its tribological properties which are inevitably connected with its microstructure (Ref 5). Recently, biomedical applications of zirconia also utilize its exceptional tribological properties. Dental and prosthetic applications also require a deep knowledge of relationship between and the microstructure and functional properties (Ref 6). Another application of zirconia as solid electrolyte also requires microstructure optimization and grain boundary engineering to achieve optimal electrical conductivity (Ref 7, 8). Zirconia as a barrier coating needs further optimization of microstructure from thermal conductivity point of view (Ref 9). In each of the applications mentioned above, controlling microstructural development plays an important role. Widely used theoretical approach to optimize zirconia sintering conditions utilizes two-dimensional description of the microstructure (e.g., Ref 10). Traditionally, microstructural characterization is based on a single planar section through the material (Ref 11). However, this does not provide all necessary information about the analyzed microstructure (Ref 12). For example, such an approach allows to determine the grain boundary trace from two-dimensional sections, but the inclination of the boundary plane to the section surface remains unknown. To overcome such a limitation, stereological methods based on probability calculations have been developed to extrapolate two-dimensional experimental results to three-dimensional space (Ref 2). Recent developments in scanning electron microscopy (SEM) enabled a direct three-dimensional (3D) analysis of ceramic microstructure as in the case of serial sectioning experiments in dual-beam SEM, carried out to investigate solid oxide fuel cell electrodes containing zirconia-based composites (Ref 13-15).

The incorporation of electron backscatter diffraction (EBSD) technique into a dual-beam FIB–SEM enables to map local crystallographic orientation in three dimensions (so-called 3D-EBSD approach). Such experimental data were used to determine a true 3D grain size and shape as well as to calculate boundary plane distributions and frequencies of occurrence for characteristic boundaries (Ref 2, 16-19). In our previous papers, we showed that it was possible to conduct 3D EBSD measurements on dense zirconia ceramics from relatively large volumes (25×10^3 m^3) avoiding detrimental electrical charging (Ref 20, 21). In this work, we show a comparison of microstructural parameters characterizing the YSZ at four different temperatures obtained from data sets acquired using two experimental approaches (2D and 3D-EBSD) which were processed utilizing three different computational methods, namely two-dimensional and three-dimensional image analysis, as well as stereological calculations.

2. Experimental

2.1 Material

A set of four samples was produced from zirconia powders containing 8 mol.% of yttria, manufactured by calcination of co-precipitated hydroxides at 773 K (500 °C). The powders of

Piotr Bobrowski and **Marek Faryna**, Institute of Metallurgy and Materials Science, Polish Academy of Sciences, Kraków, Poland; and **Zbigniew Pędzich**, Department of Ceramics and Refractory Materials, Faculty of Materials Science and Ceramics, AGH - University of Science and Technology, Kraków, Poland. Contact e-mail: m.faryna@imim.pl.

specific surface area $S_w = 70.8 \pm 0.2$ m^2/g were uniaxially compacted under pressure of 200 MPa and pressureless sintered at maximum temperatures of 1773, 1823, 1873 and 1923 K (i.e., 1500, 1550, 1600 and 1650 °C) to fabricate a series of four experimental samples with distinctly different grain sizes. The heating rate was 3 K/min (3 °C/min) and soaking time at maximum temperature was 2 h in each case. By this method, cylindrical samples of 6 mm diameter and 1 mm thickness were prepared. Samples were denoted with a number according to the maximum temperature (in Celsius) at which they were sintered. Phase analysis performed by x-ray diffraction using PANalytical Empyrean system with CuK$_{\alpha 1}$ radiation revealed that all sintered materials consisted of cubic phase only (Fig. 1).

2.2 Experimental Procedure

Prior to 3D EBSD measurements, 2D EBSD maps were acquired in low vacuum conditions at a water vapor pressure of 0.45 Torr using the EDAX Hikari camera. The operating parameters of the electron beam were as follows: An accelerating voltage was set to 20 kV, and beam current to 8 nA. Diffraction patterns were analyzed at a rate of 50-100 patterns per second. Orientation maps were acquired from 50 by 50 μm regions with square grid pattern and 200 nm step size. Prior to 3D EBSD measurements, which have to be performed in high-vacuum conditions, all compacted cylindrical samples were sputter-coated with gold to obtain a continuous, thick, conductive layer. During 3D EBSD data acquisition, the material was milled away using 30 kV and 5 nA beam of Ga$^+$ ions. Parameters of the electron beam were the same as in the case of 2D measurements, namely 20 kV and 8 nA. Ion milling enables the preparation of cross sections of high quality with smooth surfaces appropriate for EBSD measurements. This was the reason why electron diffractions were collected at relatively high rate of up to 100 fps. For all samples, the 3D EBSD maps were 40 μm wide and 20 μm high with 200 nm step size in both directions. Milling was performed 10 μm deep into the material with 200 nm slice thickness, which resulted in the acquisition of 100 EBSD maps.
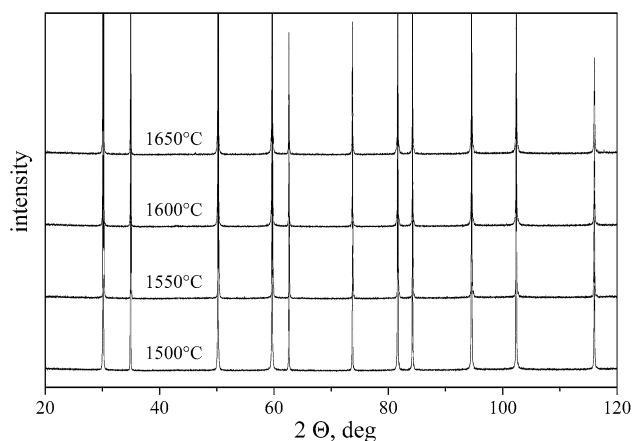

Fig. 1 XRD diffraction patterns of investigated samples. All x-ray peaks correspond to the cubic zirconia phase

2.3 Data Processing

Experimental data were processed using OIM Analysis 5.0 and Dream 3D 4.2 (Ref 22) software. Additionally, ParaView software was used for visualization. A clean-up routine utilizing grain dilation and orientation averaging was applied to the acquired EBSD data. The minimum grain size was set to 10 adjacent pixels within each map having misorientation angles lower than 2° according to Humphreys (Ref 23). Reconstructions of grain boundary networks and calculation of grain boundary density S_V were carried out using Dream 3D software utilizing the marching cube algorithm.

Stereological calculations were performed using the same EBSD data as for 2D analysis. In case of each sample, 10 vertical and 10 horizontal randomly distributed lines were drawn on the EBSD maps to measure intercept lengths. The drawing of 20 lines was necessary to count more than 200 boundary intersections (in case of the 1600 and 1650 °C samples), which was assumed to be a sufficient number for a reliable analysis. Subsequently, grain boundary densities in 3D space were calculated as follows:

$$S_V = 2 \cdot P_L \qquad (\text{Eq 1})$$

where P_L denotes the number of boundary intersection points along the drawn lines per unit length (Ref 24).

The second method to derive grain boundary density from 2D EBSD maps was to calculate the grain boundary length per unit area, which was converted into S_V using the following formula:

$$S_V = \frac{4}{\pi} \cdot L_A \qquad (\text{Eq 2})$$

where L_A denotes the length of boundary segments per unit area on the EBSD map (Ref 24).

Experimental uncertainties were estimated as standard deviations ($\pm 1\sigma$) of numbers of intersections, boundary segments and log-normal distributions.

3. Results

3.1 2D EBSD Approach

Figure 2 shows conventional 2D inverse pole figure (IPF) maps acquired from the 1500, 1550, 1600 and 1650 °C samples. Grain boundaries were marked as black lines. As expected, the IPF maps revealed the increase in grain size with the increase in sintering temperature. The 1600 and 1650 °C samples contained both large and small grains of polygonal shape. The IPF maps were partitioned into grains using a 2° misorientation angle threshold. Crystallites located at map edges were excluded from the analysis of grain size. It was assumed that grains cut by the edges of the region of interest (ROI) could bias the grain size estimation because their actual size was larger than appeared on the maps. The number of grains analyzed in each map varied from 302 to 64 for the 1500 and 1650 °C samples, respectively (Table 1). The grain area estimation was calculated by counting the number of pixels attributed to each grain and multiplying by the area of a single pixel (0.04 μm^2). For better comparison with results of 3D analysis presented later in this paper, grain areas were converted into equivalent circle diameters (ECDs). Since the analyzed samples contained equiaxed grains, it was assumed that grains can be approximated by circles according to the following formula:

$$d_2 = \sqrt{\frac{4S}{\pi}}$$ (Eq 3)

where d_2 is the equivalent diameter derived from 2D data and S—the grain area (Ref 25). Figure 3 shows the 2D grain size distributions, which were approximated by log-normal distributions. The average grain size was determined as the average value of log-normal distribution. For the 1500 °C sample (sintered at the lowest temperature), the narrowest grain size distribution (GSD) was observed with an average value of ca 3.2 µm (Table 1). GSDs for the 1600 and 1650 °C samples were both similar with regard to shape, with average values of grain diameters at ca. 5.5 µm. GSDs for the 1600 and 1650 °C samples were ranging wider compared to the values obtained for the 1500 and 1550 °C samples. The wider ranging GSDs for the samples sintered at higher temperatures resulted from the faster grain growth at elevated temperatures and preferential growth of certain crystallites at the cost of the others. These observations agreed well with the general knowledge about the sintering, i.e., ceramics sintered at a higher temperature contain much larger grains (e.g., Ref 26, 27). Grain boundary length (GBL) was calculated as the length of line segments separating particular grains on the IPF maps (Fig. 2). The minimum misorientation threshold between neighboring grains to define boundaries was set to 2

degrees. The calculated GBL varied between 2140 and 1080 µm for the 1500 and 1650 °C samples, respectively (Table 1). Grain boundary densities were obtained by calculating the ratios of boundary lengths to the areas derived from the IPF maps, i.e., 2500 µm² (50 × 50 µm), and by subsequent conversion using Eq 2. A continuous decrease in grain boundary density with the increase in sintering temperature was also observed (Table 1). The calculated values ranged from 1.09 µm²/µm³ for the 1500 °C sample to 0.55 µm²/µm³ for the 1650 °C sample.

3.2 3D EBSD Approach

Three-dimensional visualizations of grain boundary networks are shown in Fig. 4. Misorientations across boundaries were color-coded according to the legend bar. The reconstructions revealed large differences in grain size between the samples: the 1500 °C sample exhibited the smallest grains, while the 1650 °C sample had the largest crystallites. These observations agreed well with those derived from 2D data. In all visualized microstructures grain boundaries formed large, flat surfaces separating particular zirconia grains. Such microstructures are characteristic for an equilibrium state of crystal growth (Ref 28). Series of IPF maps acquired during 3D experiments were partitioned into grains using the same misorientation threshold value as in the case of 2D data, i.e., 2°. Crystallites which were
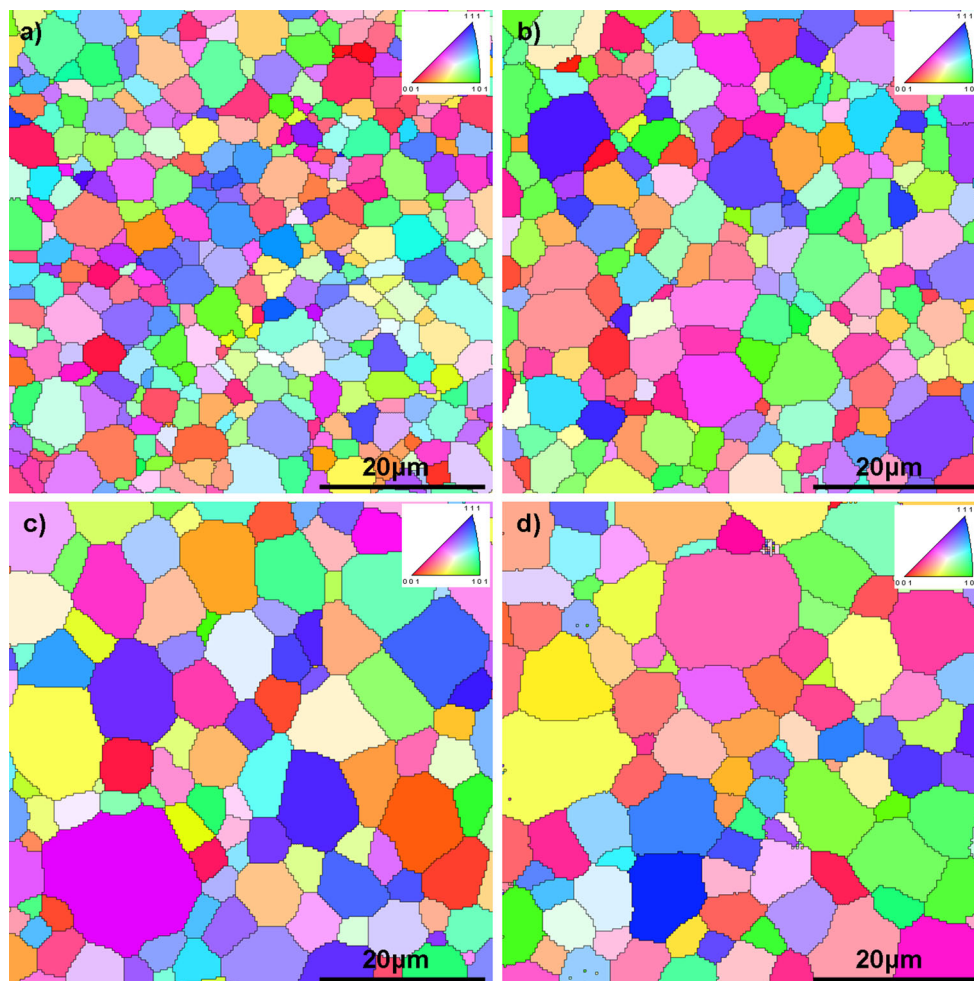

Fig. 2 2D inverse pole figure (IPF) EBSD maps acquired from: (a) 1500, (b) 1550, (c) 1600, (d) 1650 °C samples; grain boundaries were marked with black solid lines; reference triangles are visible on the upper right corner of each map

cut by the boundaries of ROI were excluded from grain size analysis. The numbers of grains decreased with the increase in sintering temperature (Table 1) from 428 for the 1500 to 52 for the 1650 °C sample suggesting a preferential growth of some grains during sintering at the cost of the others. The volumes of grains were calculated in a similar way to the 2D data, however counting of voxels was conducted for all consecutive IPF maps in the stack which contained a particular grain. Subsequently, the numbers of voxels were multiplied by their volumes (0.008 μm^3 for each case). Finally, grain volumes were converted into equivalent sphere diameters (ESDs). Based on the assumption that grain shape can be approximated by a sphere, the ESD can be calculated from the following equation:

$$d_3 = \sqrt[3]{\frac{6V}{\pi}} \qquad \text{(Eq 4)}$$

where d_3 is the equivalent sphere diameter derived from the 3D data and V—the grain volume (Ref 25). Histograms of calculated 3D grain sizes along with log-normal curves fitted to the data are shown in Fig. 5. Similarly as in the case of 2D data, the calculated EDSs were broadening with the increase in sintering temperature, reaching average values at 3.64 and 5.75 μm for the 1500 and 1650 °C samples, respectively (Table 1). The broadening of the EDSs at higher sintering temperatures results from the increase in the amount of large grains at the cost of the smaller ones.

The geometry of grain boundary networks was reconstructed from 3D data using a 'marching cube' algorithm implemented in the Dream 3D software (Ref 22). Boundaries were approximated as dense meshes of flat triangles. Grain boundary areas (GBAs) were estimated as the total areas of the triangles within the investigated volumes of material. Grain boundary densities (S_V) were calculated as the ratio of boundary area to the analyzed volume (Ref 25). A continuous decrease in S_V with the increase in sintering temperature was observed. This agrees well with the expectations as the density of grain boundaries should decrease during sintering due to the reduction of the number of grains and their continuous growth

Table 1 Microstructure parameters calculated from 2D, 3D data and stereology approach

	Sample	1500	1550	1600	1650
2D	Number of grains	302	181	66	64
	Equivalent circle diameter (ECD), μm	3.23 ± 0.53	3.85 ± 0.48	5.35 ± 0.47	5.59 ± 0.52
	Grain boundary length (GBL), μm	2140 ± 530	1680 ± 320	1180 ± 410	1080 ± 500
	Grain boundary density (S_V), $\mu m^2/\mu m^3$	1.09 ± 0.27	0.85 ± 0.17	0.60 ± 0.20	0.55 ± 0.25
3D	Number of grains	428	224	119	52
	Equivalent sphere diameter (ESD), μm	3.64 ± 0.61	4.16 ± 0.28	4.96 ± 0.18	5.75 ± 0.27
	Grain boundary area (GBA), μm^2	8850 ± 940	7600 ± 870	6500 ± 810	5710 ± 760
	Grain boundary density (S_V), $\mu m^2/\mu m^3$	1.11 ± 0.12	0.95 ± 0.11	0.81 ± 0.10	0.71 ± 0.09
Stereology	Number of intercepts	400	293	215	215
	Mean intercept length, μm	2.46 ± 0.37	3.38 ± 0.83	4.61 ± 0.82	4.56 ± 0.95
	Grain boundary density (S_V), $\mu m^2/\mu m^3$	0.81 ± 0.12	0.59 ± 0.14	0.43 ± 0.08	0.44 ± 0.09

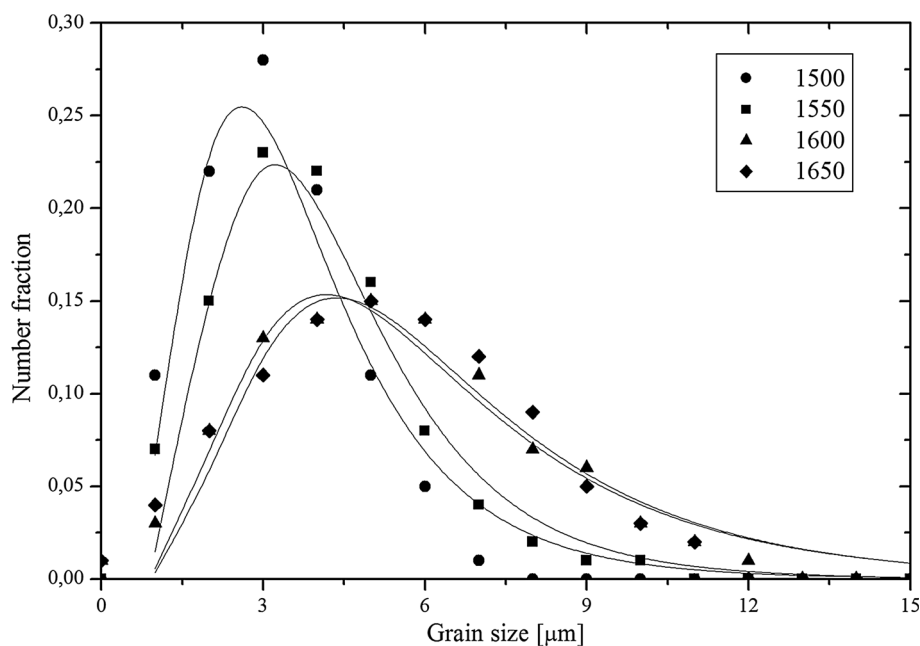Uncertainties were estimated as standard deviations ($\pm 1\sigma$)

Fig. 3 Grain size distributions calculated from 2D EBSD data. Continuous lines show log-normal curves fitted to experimental data

(Ref 29). It has to be mentioned that at this stage the investigated volumes of material were insufficient for statistically reliable analysis of both grain boundary character and grain boundary energy distributions.

3.3 Stereological Approach

Stereological calculations were based on 20 lines drawn randomly on the EBSD maps. The obtained mean intercept lengths ranged from 2.46 to 4.56 μm, and the calculated grain
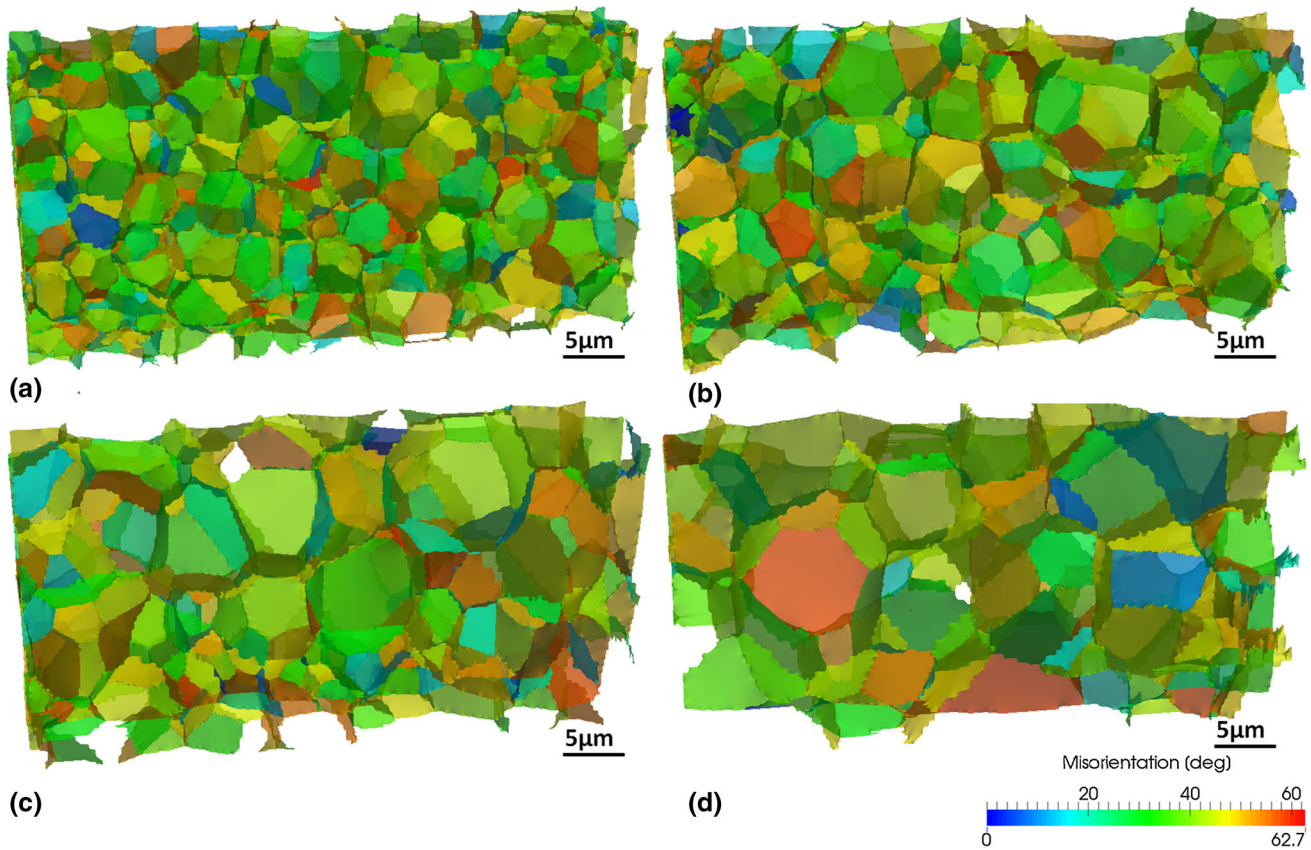

Fig. 4 3D visualizations of grain boundary networks in: (a) 1500, (b) 1550, (c) 1600 and (d) 1650 °C samples. Misorientation between neighboring grains is color-coded according to the legend bar
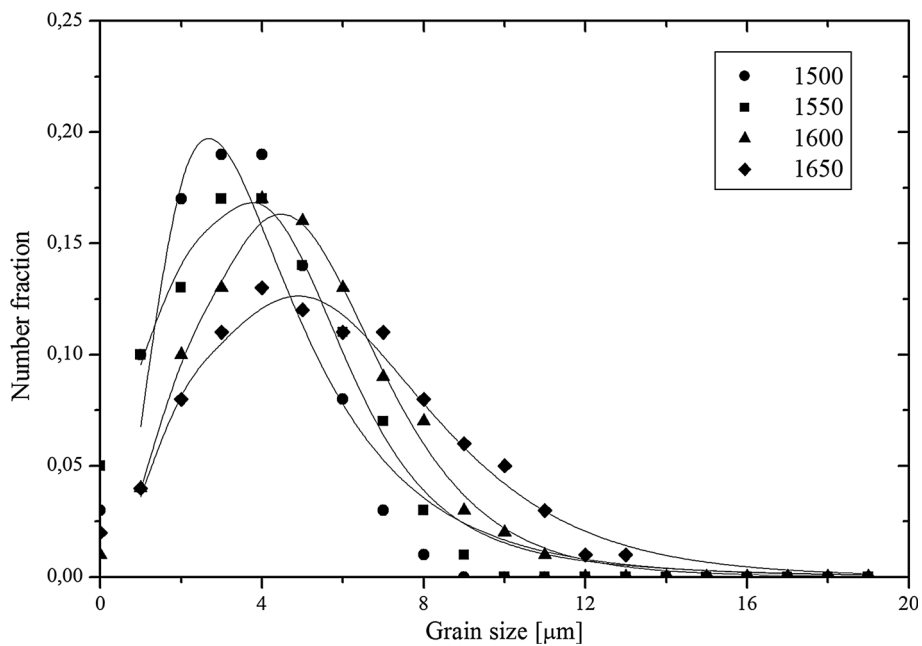

Fig. 5 Grain size distributions calculated from 3D EBSD data. Continuous lines show log-normal curves fitted to experimental data

boundary densities varied between 0.81 and 0.43 μm²/μm³ for the 1500 and 1600 °C samples, respectively.

4. Discussion

Both 2D and 3D results revealed that all analyzed samples contained equiaxed grains. The wide spread of grain sizes observed in Fig. 2(c) and (d) might suggest a bimodal grain diameter distribution for the 1600 and 1650 °C samples. However, this observation was neither confirmed by grain size distributions shown in Fig. 3 nor by 3D EBSD results (Fig. 4 and 5). Such a misleading conclusion comes from the fact that 2D IPF maps represent random sections through particular grains. Cutting the grains with random sections results in a broad distribution of cross-section areas as well as grain diameters. Furthermore, the calculations of ECDs based on statistical approach revealed that the distributions for 1600 and 1650 °C samples contained single maxima only.

The calculated average ESD values for all samples were similar to those obtained by Helmick et al. (Ref 2) for the comparable material and methodology. The comparison of ECDs and ESDs shown in Fig. 6 revealed a good agreement between grain diameters calculated by the 2D and 3D approach. Mean intercept length values were comparable to those obtained by Yoshizawa (Ref 11). Although the mean intercept lengths ECDs and ESDs are not directly comparable, as the first one refers to the average random secant of a grain while the two other denote its maximum values, it may be worth knowing the relationship between these values. As expected, the mean intercept lengths were shorter compared to the ECDs and ESDs and were about 80% of the average diameter values.

A comparison of grain boundary densities calculated using different methods is shown in Fig. 7. According to the Cavalieri-Hacquert principle applied to grain boundaries (Ref 25), the S_V calculated by all three methods, i.e., 2D EBSD and 3D EBSD techniques and stereological approach, should be comparable. However, the results of 3D analysis were noticeably higher compared to two other approaches. When compar-
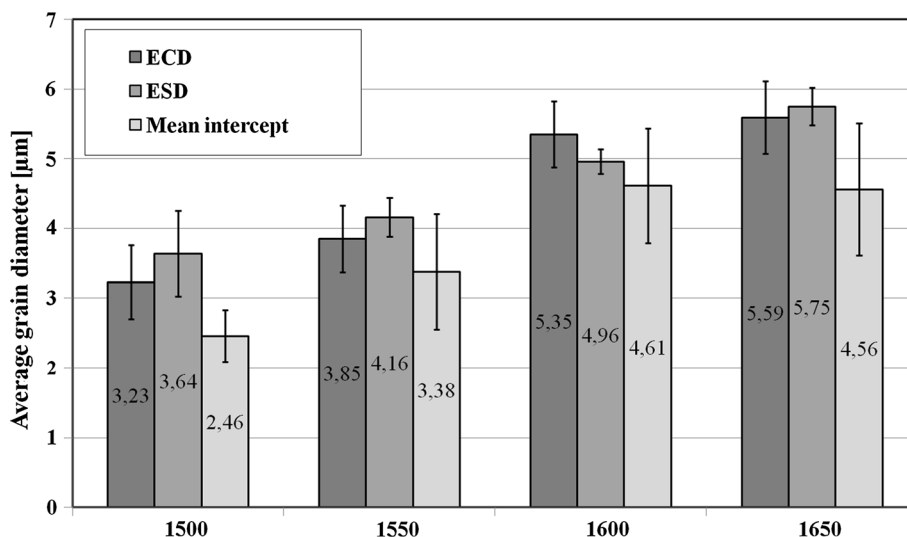

Fig. 6 Calculated average grain diameters based on 2D and 3D EBSD data and stereological approach with ±1σ error bars
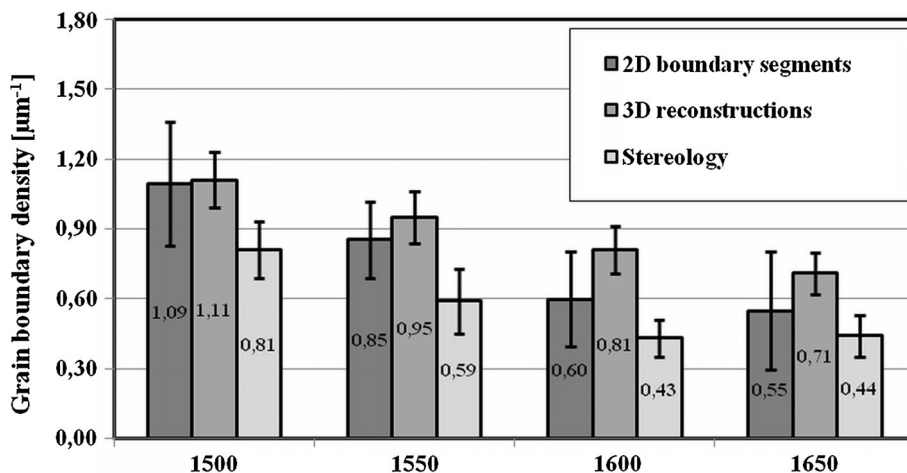

Fig. 7 Calculated grain boundary densities based on 2D and 3D EBSD data and stereological approach with ±1σ error bars

ing the results of 2D EBSD to 3D EBSD analysis, the obtained values agreed within ranges of experimental uncertainty ($\pm 1\sigma$), but in case of stereological approach the obtained values were significantly different. Bearing in mind that the shapes of grains measured in 3D are much closer to reality, it is assumed that the microstructure parameters (e.g., S_V) are also more reliable than the values obtained by stereological approach. Summarizing, it must be stated that all three analytical approaches revealed similar trends, i.e., that the grain boundary densities were reduced along with the increase in the sintering temperature with a tendency that the 3D EBSD and 2D EBSD data delivered more accurate and reliable results.

5. Conclusions

The analysis of the results obtained by use of the 2D and 3D EBSD technique and stereological approach from cubic zirconia samples revealed noticeable differences between the values of calculated microstructural parameters. In case of grain size, the 2D and 3D analysis yielded similar results; however, the grain size values obtained from the stereological approach were about 20% lower than the ECD and ESD values. In case of the S_V, experimental results indicate that the 2D and 3D data are quite comparable. However, stereological analysis yielded the S_V values noticeably lower than those obtained from 2D and 3D EBSD data. Though a comparison of the results obtained by use of the 2D and 3D EBSD technique and stereological approach of the cubic zirconia samples revealed several differences between the values of calculated microstructural parameters, a general trend regarding the evolution of average grain sizes and grain boundary densities upon increase of the sintering temperature remains the same for all three approaches. Higher pressureless sintering temperature leads to the formation of ceramics containing much lower number of larger grains and, consequently, lower density of grain boundaries. These observations agree well with common knowledge about sintering of ceramics.

References

1. H. Beladi and G. Rohrer, The Relative Grain Boundary Area and Energy Distributions in a Ferritic Steel Determined from Three-Dimensional Electron Backscatter Diffraction Maps, *Acta Mater.*, 2013, **61**, p 1404–1412

2. L. Helmick, S. Dillon, K. Gerdes, R. Gemmen, G. Rohrer, S. Seetharaman, and P. Salvador, Crystallographic Characteristics of Grain Boundaries in Dense Yttria-Stabilized Zirconia, *Intl. J. Appl. Ceram. Technol.*, 2011, **8**, p 1218–1228

3. Z. Xia, B. Chen, and K. Lu, 3D Microstructure Construction and Quantitative Evaluation of Sintered ZrO_2 Under Different Sintering Conditions, *J. Mater. Sci.*, 2013, **48**, p 5852–5861

4. A. Wojteczko, R. Lach, K. Wojteczko, and Z. Pędzich, Investigation of Subcritical Crack Growth Phenomenon and Estimation of Life Time of Alumina and Alumina–Zirconia Composites with Different Phase Arrangement, *Ceram. Int.*, 2016, **42**, p 9438–9442

5. B. Basu, J. Vleugels, and O. Van Der Biest, Microstructure–Toughness–Wear Relationship of Tetragonal Zirconia Ceramics, *J. Eur. Ceram. Soc.*, 2004, **24**, p 2031–2040

6. M. Fornabaio, P. Palmero, R. Traverso, C. Esnouf, H. Reveron, J. Chevalier, and L. Montanaro, Microstructure–Toughness–Wear Relationship of Tetragonal Zirconia Ceramics, *J. Eur. Ceram. Soc.*, 2015, **35**, p 4039–4049

7. C. Zhang, C.-J. Li, G. Zhang, X.-J. Ning, C.-X. Li, H. Liao, and C. Coddet, Ion Conductivity and Its Temperature Dependence of Atmospheric Plasma-Spayed Yttria Stabilized Zirconia Electrolyte, *Mater. Sci. Eng. B*, 2007, **137**, p 24–30

8. A. Pawłowski, M.M. Bućko, and Z. Pędzich, Microstructure Evolution and Electrical Properties of Yttria and Magnesia Stabilized Zirconia, *Mater. Res. Bul.*, 2002, **37**, p 425–438

9. Y. Wang and Ch Zhou, Microstructure and Thermal Properties of Nanostructured Gadolinia Doped Yttria-Stabilized Zirconia Thermal Barrier Coatings Produced by Air Plasma Spraying, *Ceram. Int.*, 2016, **42**, p 13047–13052

10. V. Pouchly and K. Maca, Sintering Kinetic Window for Yttria-Stabilized Cubic Zirconia, *J. Eur. Ceram. Soc.*, 2016, **36**, p 2931–2936

11. Y. Yoshizawa and T. Sakuma, Evolution of Microstructure and Grain Growth in ZrO_2-Y_2O_3 Alloys, *ISIJ Int.*, 1989, **29**, p 746–752

12. G. Rohrer, J. Li, S. Lee, A. Rollett, M. Groeber, and M. Uchic, Deriving Grain Boundary Character Distributions and Relative Grain Boundary Energies from Three-Dimensional EBSD Data, *Mater. Sci. Technol.*, 2010, **26**, p 661–669

13. J. Wilson, W. Kobsiriphat, R. Mendoza, H. Chen, J. Hiller, D. Miller, K. Thornton, P. Voorhees, S. Adler, and S. Barnett, Three-Dimensional Reconstruction of a Solid Oxide Fuel Cell Anode, *Nat. Mater.*, 2006, **5**(7), p 541–544

14. H. Iwai, N. Shikazono, T. Matsui, H. Teshima, M. Kishimoto, R. Kishida, D. Hayashi, K. Matsuzaki, D. Kanno, M. Saito, H. Muroyama, K. Eguchi, N. Kasagi, and H. Yoshida, Quantification of SOFC Anode Microstructure Based on Dual Beam FIB–SEM Technique, *J. Power Sources*, 2010, **195**, p 955–961

15. S. Dillon, L. Helmick, H. Miller, L. Wilson, R. Gemman, R. Petrova, K. Barmak, G. Rohrer, and P. Salvador, The Orientation Distributions of Lines, Surfaces, and Interfaces around Three-Phase Boundaries in Solid Oxide Fuel Cell Cathodes, *J. Am. Ceram. Soc.*, 2011, **94**, p 4045–4051

16. S. Dillon and G. Rohrer, Characterization of Grain-Boundary Character and Energy Distributions of Yttria Using Automated Serial Sectioning and EBSD in the FIB, *J. Am. Ceram. Soc.*, 2009, **92**, p 1580–1585

17. A. Morawiec and K. Głowiński, On "Macroscopic" Characterization of Mixed Grain Boundaries, *Acta Mater.*, 2013, **61**, p 5756–5767

18. K. Głowiński and A. Morawiec, Towards Effective Analysis of Large Grain Boundary Data Sets, *IOP Conf. Ser. Mater. Sci. Eng.*, 2015, **82**, p 012085

19. K. Głowiński and A. Morawiec, Analysis of Experimental Grain Boundary Distributions Based on Boundary-Space Metrics, *Metal. Mater. Trans. A*, 2014, **45**, p 3189–3194

20. P. Bobrowski, M. Faryna, and Z. Pędzich, Investigation of Grain-Boundary Geometry and Pores Morphology in Dense and Porous Cubic Zirconia Polycrystals, *Mater. Res. Bull.*, 2014, **57**, p 203–209

21. P. Bobrowski, Z. Pędzich, and M. Faryna, Three-Dimensional Microstructural Characterization Of Porous Cubic Zirconia, *Micron*, 2015, **78**, p 73–78

22. M. Groeber and M. Jackson, DREAM.3D: A Digital Representation Environment for the Analysis of Microstructure in 3D, *Integr. Mater. Manuf. Innov.*, 2014, **3**, p 5

23. F. Humphreys, Grain and Subgrain Characterisation by Electron Backscatter Diffraction, *J. Mater. Sci.*, 2001, **36**, p 3833–3854

24. A. Baddeley and E.B.V. Jensen, *Stereology for Statisticians*, Chapman & Hall/CRC, A CRC Press Company, Boca Raton, 2005, p 19–23
25. J.E. Hillard and L.R. Lawson, *Stereology and Stochastic Geometry*, Kluwer Academic Publishers, Dordrecht, 2003, p 247–248
26. C. Sagel-Ransijn, A. Winnubst, A. Burggraaf, and H. Verweij, Grain Growth in Ultrafine-Grained Y-TZP Ceramics, *J. Eur. Ceram. Soc.*, 1997, **17**, p 1133–1141
27. B. Xia, L. Duan, Y. Xie, and Y. Tang, Preparation of Y_2O_3 Stabilized ZrO_2 Ceramic Nanopowders By Surface Doping, *Mater. Sci. Technol.*, 1999, **15**, p 755–760
28. S. Smith, Grains, Phases, and Interfaces—An Interpretation of Microstructure, *Trans. AIME*, 1948, **175**, p 15–51
29. A. Ferrero and M. Fortes, The Elimination of Grains and Grain Boundaries in Grain Growth, *Interface Sci.*, 1997, **5**, p 263–278